Review Article

Marc Gronle* and Wolfgang Osten

Multi-scale referencing and coordinate unification of optical sensors in multi-axis machines

Abstract: Multi-scale optical sensor systems help to overcome the area of conflict between resolution, field size, and inspection time if it comes to the frequent problem of detecting small defects on large areas. The sensors of such systems are chosen according to two main properties: On the one hand, they should measure in opposed scales; on the other hand, their measurement principles should vary as well in order to be suitable for different material and surface properties. However, these systems can only operate at full capacity if it is possible to unify the acquired data from each sensor into one common coordinate system such that an overall analysis is possible, or subsequent sub-measurements can be triggered. In this paper, a general approach for a common sensor referencing is proposed, whose focus lies on microscopic optical sensors for both scattering and reflecting surfaces. The method is able to handle resolutions from the nanometer to millimeter scale in one single system, but is also feasible for a coordinate unification across several single sensor systems.

1 Introduction

The visible trend in major key technologies such as biotechnology, microelectronics and production technology is the continuous improvement of the manufacturing precision as well as the massive reduction of feature sizes at

*Corresponding author: Marc Gronle, Institut für Technische Optik, Universität Stuttgart, Pfaffenwaldring 9, 70569 Stuttgart, Germany, e-mail: gronle@ito.uni-stuttgart.de
Wolfgang Osten: Institut für Technische Optik, Universität Stuttgart, Pfaffenwaldring 9, 70569 Stuttgart, Germany

both very small and large components [1]. Additionally, the market has been changed within the last decades to a flexible, on-demand production based on individual requirements of every customer. These trends also call for a growing demand for consistent quality control, requiring fast, reliable, and flexible inspection systems. On the one hand, such systems must handle many types of objects that vary in shape, size, and material properties. On the other hand, flexible optical inspection systems have to be able to inspect small defects on large objects, which can, for instance, be measured by the area-related resolution [2] defined by the quotient of the lateral feature size and the object's extension.

The first aspect of varying types of objects is already important concerning the choice of the applied optical sensor(s). It might already be necessary to install different types of sensors in order to acquire multi-modal information, for instance, to both measure the color and shape [3] or local height and slope value of objects [4]. Depending on different material properties and resolution requirements, it will be inevitable to sequentially use different measurement principles, like confocal sensors, white-light interferometers or triangulation-based devices using both structured light illumination or deflectometry [5, 6].

Besides applying different optical sensors to provide a multi-modal measurement, approaches need to be found to efficiently detect small defects on large areas. Solutions for this inspection task can mainly be categorized in three groups with respect to the choice and number of optical sensors [7–10]. At first, it is possible to scan the entire object with a single sensor system and appropriate resolution to meet the requirements for detecting the small defects. This is usually realized in many optical desktop measurement systems using the built-in stitching features. This method is required if the entire surface needs to be completely sampled with a constant and high resolution, but needs a lot of acquisition time. To improve the speed, systems have been proposed that consist of a parallel arrangement of many duplicated sensors. This has, for instance, been shown for the inspection of microelectromechanical systems (MEMS) and microoptoelectromechanical systems (MOEMS) on a wafer level [11]. The most flexible approach,

however, is the application of multi-scale sensor systems with various types of optical sensors [5]. The idea is to equip an inspection system with a hierarchical set of different optical sensors, working in several scales, hence, inverse combinations of resolution and field sizes. An overview analysis of the inspected part is then observed in a low scale by a coarsely resolving sensor, while high-resolution sensors are iteratively applied only to subregions of interest. An example of a multi-scale inspection system of automotive parts based on various fringe projection sensors has been introduced by Kayser et al. [12]. Later, these systems were modified for the flexible inspection of wafers with a focus on the automatic selection of appropriate sensors [13, 14]. While the field sizes of the mentioned systems lie in the range of several microns up to a few centimeters, multi-scale approaches have also been reported for systems with object sizes up to several meters under the name 'large-scale dimensional metrology' [15] and also for flexibelly inspecting defects in the centimeter range on objects with a size in the range of 1 m using a single, a stereo, as well as a laser camera [16].

The presented multi-sensor and multi-scale setups can only unfold their real power if they are mounted on a precise multi-axis machine that allows repositioning any sensor to desired areas of the large object under inspection. However, data acquired at varying positions and by different sensors can only be fused with respect to their geometry or other properties, if all sensors as well as the available axes are registered with respect to one single machine coordinate system. Then, the sensor data are transformed into this common coordinate system, where the inspection or determination of subsequent measurement steps, using more precise sensors, is executed [6]. Optionally, data fusion and reduction processes can be applied to improve the overall data set, e.g. for a general comparison with a given model. This sub-step, however, is only possible in terms of robustness if large overlapping areas are available, and the single measured patches have unique features [17].

In the literature, one can find many approaches for data fusion in multi-sensor setups with the common goal to get all acquired data in one single coordinate system. Multiple methods propose to use iterative closest point (ICP) algorithms or similar methods in order to match one data set with another one [18, 19]. However, these approaches are more suitable for data sets obtained by the same or at least homogeneous sensors (concerning their resolution and data type). In the case of a general system of multi-scale optical sensors, this is difficult as it has to be possible to align, for instance, data from a $50\times$ white-light interferometer with a measurement from a microscopic fringe projection with a lateral extent of

15 mm. Other approaches try to solve the coordinate unification problem of various sensors by measuring reference objects. Usually, three selected datum points are sufficient to solve the geometric transformation from one sensor to another one. For high-precision results, ball plates are used as reference objects that consist of three or more high-precision spheres, which can be measured both by tactile as well as optical instruments. The datum points are then obtained by the center of the fitted spheres [20, 21]. In many cases, it is possible to adjust the form and shape of a reference specimen to the field size, resolution, and material constraints of applied sensors. Loderer and Hausotte [17] presented a multi-fringe projection system for the analysis of large objects where every sensor is focused on another part of the surface. The sensor registration is then executed with a matt reference specimen that can be simultaneously measured by all sensors and has uniquely shaped 3D markers on the surface to identify the sensor's position and orientation.

In this paper, a general approach for the coordinate unification of multi-scale optical sensor systems, mounted in precise multi-axis machines is presented. This method should be applicable to systems equipped with different microscopic optical sensors, whose field size lies in a range between 100 μm and a few centimeters. Additionally, the sensors can have opposed fields of applications concerning the surface characteristics of the measured objects: a fringe projection sensor is only capable of measuring scattering surfaces, while a white-light interferometer (WLI) or confocal sensor is able to also register the surface of reflecting objects. Furthermore, the referencing approach is also able to take the position and orientation of translational axes of the multi-axis machine into account such that the data referencing is possible, even if the object or a sensor has been moved to different positions.

2 Multi-sensor coordinate unification

The presented coordinate unification method for multiple 2.5D or 3D optical sensors in a multi-axis machine is based on the schematic in Figure 1. Usually, it is assumed that all sensors are mounted at the same end effector, such that one set of x, y, and z axes can move every sensor to a single point on an object's surface. However, the approach also allows an overall referencing across single desktop sensors systems, all having their own stages. Owing to this more general approach, a few more coordinate systems have to be defined, and some coordinate frames are indicated with
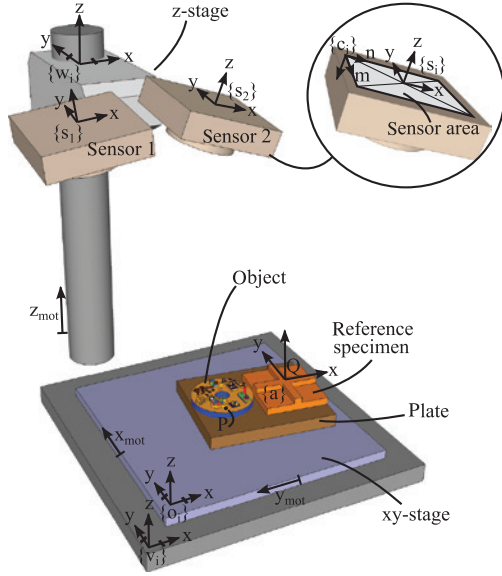
Figure 1: Schematic of a multi-axis machine with up to three translational axes and n sensors. An object with any surface point P is located on the x-y stage and stationary with respect to a reference specimen. If all sensors are mounted in the same system, the coordinate systems $\{w_i\}$, $\{v_i\}$, and $\{o_i\}$ are identical. However, to keep the setup as general as possible, the sensors can also be located in separate setups with their own stationary coordinate systems. Only the frame $\{a\}$ is always identical.

the indices i representing each desktop sensor system. In the default case, these coordinate systems are identical for all sensors. The multi-axis machine can be equipped with up to three translational axes x, y, and z that are assumed to be perpendicular to each other. Furthermore, all axes are considered to be good enough to provide linear movements with irrelevant positioning uncertainties.

The coordinate systems or frames are defined as follows:
- $\{a\}$ is the Cartesian frame of a reference specimen with its center point $_aQ$. This is the unified coordinate system to which all acquired data should be transformed to.
- $\{o_i\}$ is a Cartesian frame of a sensor i, stationary with respect to an x-y stage. Its axes are parallel to the x- and y-axes.
- $\{v_i\}$ is the Cartesian coordinate system that is only translated from $\{o_i\}$ and assumed to be fixed to the machine base.
- $\{w_i\}$ is a Cartesian coordinate system that is only translated from $\{v_i\}$ by the movement of the z-axis.
- $\{s_i\}$ is a Cartesian coordinate system for each sensor i. It is fixed with respect to $\{w_i\}$.
- $\{c_i\}$ is an optional, arbitrary coordinate system, that is located in the sensor area and represents the imaging sensor coordinates (in pixels).

Any point $P(x, y, z)$ can be defined with respect to an arbitrary coordinate system $\{k\}$, which is denoted by $_kP$. A transformation from point P from one frame $\{k\}$ o to another frame $\{j\}$ is described in homogeneous coordinates by a 4×4 transformation matrix $_jT_k$:

$$\begin{pmatrix} _jP \\ 1 \end{pmatrix} = {_jT_k}\begin{pmatrix} _kP \\ 1 \end{pmatrix} = \begin{pmatrix} _jR_k & _jt_k \\ \mathbf{0} & 1 \end{pmatrix}\begin{pmatrix} _kP \\ 1 \end{pmatrix} \tag{1}$$

where $_jR_k$ is a 3×3 rotation matrix, and $_jt_k$ is a translation vector. To simplify the following notations, the vector $(_jP \ \ 1)^T$, that is the point $_jP$ in homogeneous coordinates, will be written as $_jP$ below.

Based on the definitions of the different coordinate systems, the following equations hold to finally transform data, acquired in frame $\{c_i\}$, to the unified frame $\{a\}$:

$$_{s_i}P = \begin{pmatrix} \mathrm{diag}(s_{x_i}, s_{y_i}, s_{z_i}) & _{s_i}t_{c_i} \\ \mathbf{0} & 1 \end{pmatrix}{_{c_i}P} \tag{2}$$

where $(s_{x_i}, s_{y_i}, s_{z_i})$ indicates the known scaling from pixel to metric scales including an optional inversion of the axes. $_{s_i}t_{c_i}$ is the translation from the origin of the sensor area to the origin of $\{s_i\}$ that is assumed to be in the center of that area. The z-component of the translation vector can be used to indicate an additional offset, for instance, if the sensor is internally movable to a certain start position (e.g. by the use of a piezo actuator). The next transformation to frame $\{w_i\}$ is given by:

$$_{w_i}P = {_{w_i}T_{s_i}} \cdot {_{s_i}P} \tag{3}$$

The transformation matrix $_{w_i}T_{s_i}$ is hereby currently unknown. The subsequent frames $\{w_i\}$, $\{v_i\}$, and $\{o_i\}$ are only translated to each other, where the translation is only defined by the current positions of the three translational axes x_{mot}, y_{mot}, and z_{mot}:

$$_{o_i}P = {_{o_i}T_{w_i}}\big|_{q_i} \cdot {_{w_i}P} = \begin{pmatrix} \mathbf{I} & q_i \\ \mathbf{0} & 1 \end{pmatrix} \cdot {_{w_i}P} \tag{4}$$

with the joint vector

$$q_i = (\alpha_i \cdot x_{\mathrm{mot}}, \beta_i \cdot y_{\mathrm{mot}}, \gamma_i \cdot z_{\mathrm{mot}}) \tag{5}$$

where α_i, β_i, and $\gamma_i \in \{-1, 1\}$ indicate the positive direction of each motor axis. Finally, the last missing transformation to the common object's frame $\{a\}$ is given by:

$$_aP = {_aT_{o_i}} \cdot {_{o_i}P}. \tag{6}$$

Let us now define that the frame $\{a\}$ with its origin $_aQ$ is located at a clearly identifiable position of a reference

specimen. If a sensor i is moved to a position $q_{i,0}$ such that Q can be measured in frame $\{s_i\}$, its transformation to frame $\{a\}$ will be:

$$0 = {}_aQ = {}_a\boldsymbol{T}_{o_i} \cdot {}_{o_i}\boldsymbol{T}_{w_i}\big|_{q_{i,0}} \cdot {}_{w_i}\boldsymbol{T}_{s_i} \cdot {}_{s_i}\boldsymbol{Q}\big|_{q_{i,0}} \tag{7}$$

$$0 = {}_aQ = {}_a\boldsymbol{R}_{o_i}({}_{w_i}\boldsymbol{R}_{s_i} \cdot {}_{s_i}Q\big|_{q_{i,0}} + \\ {}_{w_i}\boldsymbol{t}_{s_i} + \boldsymbol{q}_{i,0}) + {}_a\boldsymbol{t}_{o_i} \tag{8}$$

Equation 8 can also be expressed for any general point ${}_a\boldsymbol{P}$, registered at the axes joint vector $\boldsymbol{q}_i$:

$$_a P = {}_a\boldsymbol{R}_{o_i}({}_{w_i}\boldsymbol{R}_{s_i} \cdot {}_{s_i}P\big|_{q_i} + \\ {}_{w_i}\boldsymbol{t}_{s_i} + \boldsymbol{q}_i) + {}_a\boldsymbol{t}_{o_i} \tag{9}$$

Subtracting eq. 8 from eq. 9 yields then the final relation to convert any registered point in a sensor's coordinate system to the common frame $\{a\}$

$$_a P = {}_aP - 0 = {}_aP - {}_aQ \\ = {}_a\boldsymbol{R}_{o_i}[{}_{w_i}\boldsymbol{R}_{s_i}({}_{s_i}P - {}_{s_i}Q\big|_{q_{i,0}}) + q_i - q_{i,0}] \tag{10}$$

The final transformation ${}_a\boldsymbol{T}_{s_i}$ is then:

$$_a\boldsymbol{P} = \begin{pmatrix} {}_a\boldsymbol{R}_{o_i}\,{}_{w_i}\boldsymbol{R}_{s_i} & {}_a\boldsymbol{R}_{o_i}\cdot\boldsymbol{x} \\ \boldsymbol{0} & 1 \end{pmatrix} \cdot {}_{s_i}\boldsymbol{P} \tag{11}$$

with $\qquad \boldsymbol{x} = -\,{}_{w_i}\boldsymbol{R}_{s_i} \cdot {}_{s_i}Q\big|_{q_{i,0}} + q_i - q_{i,0}$

According to eq. 11, the necessary components to unify different acquired sets of data from various sensors in the common frame $\{a\}$ are:

– The position of a reference marker Q at a position vector $\boldsymbol{q}_{i,0}$, acquired during the referencing process,
– the currently acquired points ${}_{s_i}\boldsymbol{P}$ including their position vector $\boldsymbol{q}_i$,
– the unknown rotation ${}_{w_i}\boldsymbol{R}_{s_i}$ between frames $\{s_i\}$ and $\{w_i\}$, which is the rotation between the sensor and the machine base including the three translational axes,
– the unknown rotation ${}_a\boldsymbol{R}_{o_i}$ between the frame $\{o_i\}$ of the x-y stage and the object's plate (only necessary for distinct desktop sensor systems).

The last unknown rotation ${}_a\boldsymbol{R}_{o_i}$ is only necessary if every sensor has its own axes. If all sensors are mounted on a single and precise multi-axis machine, this rotation can be set to the identity matrix, as it is constant for all sensors, and the relative distances between all measured surface points are invariant to an overall rotation. Figure 2 shows the overall sequence that has to be done in order to reference all desired sensors and start the real measurement.
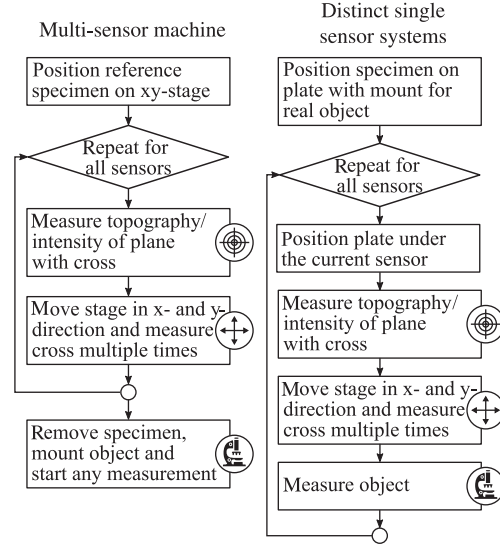
Figure 2: Scheme of the overall referencing and the subsequent measurement. The sequence is slightly different if it is applied to several distinct sensor systems or if it is used in a multi-sensor setup with one common positioning system.

The general approach is equal for both a multi-sensor setup, where all sensors are mounted on the same multi-axis actuator or a unification across distinct desktop sensor systems. Nevertheless, there are a few differences in the order of the blocks and an additional step for the single-sensor scheme. An example for such a demonstrator with one precise multi-axis machine include various sensors, like a zoomable fringe projection microscope as well as a chromatic confocal point sensor, which can be seen in Figure 3 [22].

2.1 Determination of the rotation between sensor and the machine base

To obtain the missing rotation matrix ${}_{w_i}\boldsymbol{R}_{s_i}$ between the sensor and a fixed coordinate system $\{w_i\}$ with respect to the z-axis and the x-y stage, it is required to measure a known point Q on the reference specimen multiple times while laterally moving the specimen both in the x and y direction. Using eqs. 3 and 4, the measured point Q at a position q_j is given in frame $\{o_i\}$ by:

$$_{o_i}\boldsymbol{Q} = {}_{o_i}\boldsymbol{T}_{w_i}\big|_{q_j}\,{}_{w_i}\boldsymbol{T}_{s_i} \cdot {}_{s_i}\boldsymbol{Q}\big|_{q} \tag{12}$$

$$_{o_i}\boldsymbol{Q} = {}_{w_i}\boldsymbol{R}_{s_i}\,{}_{s_i}Q\big|_{q_j} + {}_{w_i}\boldsymbol{t}_{s_i} + {}_{o_i}\boldsymbol{t}_{w_i}\big|_{q_j} . \tag{13}$$

As both the translation vector ${}_{w_i}\boldsymbol{t}_{s_i}$ and ${}_{o_i}Q$ are constant during all measurements of a single sensor, eq. 13 can be simplified to:

Figure 3: Exemplary picture of a multi-scale inspection system equipped with a zoomable fringe projection microscope and a chromatic confocal point sensor.

$$_{w_i}\boldsymbol{R}_{s_i} \cdot \, _{s_i}Q|_{q_j} = \text{const.} - \, _{o_i}\boldsymbol{t}_{w_i}|_{q_j} \tag{14}$$

In order to get rid of the constant part, it is possible to subtract Q, acquired at the first position $\boldsymbol{q}_1$, from all n ($n >= 4$) measurements. This yields a system of linear equations:

$$_{w_i}\boldsymbol{R}_{s_i} \cdot \underbrace{[\Delta\boldsymbol{Q}_2 \cdots \Delta\boldsymbol{Q}_n]}_{A} = -\underbrace{[\Delta\boldsymbol{t}_2 \cdots \Delta\boldsymbol{t}_n]}_{B} \tag{15}$$

$$\text{with } \Delta\boldsymbol{Q}_j = \, _{s_i}\boldsymbol{Q}|_{q_j} - \, _{s_i}\boldsymbol{Q}|_{q_1}$$

$$\text{and } \Delta\boldsymbol{t}_j = \, _{o_i}\boldsymbol{t}_{w_i}|_{q_j} - \, _{o_i}\boldsymbol{t}_{w_i}|_{q_1}$$

The desired rotation matrix is then determined by

$$_{w_i}\boldsymbol{R}_{s_i} = -\boldsymbol{B}\cdot\boldsymbol{A}^{-1} \tag{16}$$

where both $\boldsymbol{A}$ and $\boldsymbol{B}$ have full rank, as the movement is executed both in the x and y directions. However, if both matrices $\boldsymbol{A}$ and $\boldsymbol{B}$ contain insecure measurement values, the resulting matrix $_{w_i}\boldsymbol{R}_{s_i}$ may not be orthonormal with a determinant of 1 like what is required for rotation matrices between Cartesian coordinate systems. However, Kabsch [23] proposes an algorithm for finding the optimal rotation matrix that minimizes the root mean squared deviation between two paired sets of vectors. This algorithm is applied to obtain the desired rotation matrix.

2.2 Determination of the rotation between plate and the machine base

If the coordinate unification has to be done across distinct desktop sensor systems with their own axes, the rotation $_a\boldsymbol{R}_{o_i}$ between the arbitrarily positioned plate, containing both the reference specimen as well as the object, and the machine base $\{\boldsymbol{o}_i\}$, has to be determined. Else, this step can be ignored, and the rotation can be set to the identity matrix without loss of generality.

In order to obtain the real rotation matrix, a reference specimen is necessary where at least three distinct and known points are measurable. Then, the alignment of frame $\{\boldsymbol{a}\}$ with respect to these points can be determined. Let us assume that one of those points is the origin of frame $\{\boldsymbol{a}\}$ and the two other points lie on the x and y axis of this coordinate system. The z axis can then be derived from the cross product of x and y. Using eq. 11, the rotation between a vector $_a\boldsymbol{e}$, defined in frame $\{\boldsymbol{a}\}$ and the same vector $_{s_i}\boldsymbol{e}$, given in the coordinate system $\{\boldsymbol{s}_i\}$, is described by

$$_a\boldsymbol{e} = \, _a\boldsymbol{R}_{o_i} \cdot \, _{w_i}\boldsymbol{R}_{o_i} \cdot \, _{s_i}\boldsymbol{e} \tag{17}$$

where $_{w_i}\boldsymbol{R}_{o_i}$ is already known. If the three measured vectors $_{s_i}\boldsymbol{x}$, $_{s_i}\boldsymbol{y}$, and $_{s_i}\boldsymbol{z}$ are unit vectors and span an orthonormal basis $\{\boldsymbol{a}\}$, this equation is extendable to the following system of linear equations:

$$[_a\boldsymbol{x}, \, _a\boldsymbol{y}, \, _a\boldsymbol{z}] = \, _a\boldsymbol{R}_{o_i} \cdot \, _{w_i}\boldsymbol{R}_{s_i} \cdot [_{s_i}\boldsymbol{x}, \, _{s_i}\boldsymbol{y}, \, _{s_i}\boldsymbol{z}] \tag{18}$$

$$\begin{aligned} \boldsymbol{I} &= \, _a\boldsymbol{R}_{o_i} \cdot \, _{w_i}\boldsymbol{R}_{s_i} \cdot [_{s_i}\boldsymbol{x}, \, _{s_i}\boldsymbol{y}, \, _{s_i}\boldsymbol{z}] \\ _a\boldsymbol{R}_{o_i} &= [_{s_i}\boldsymbol{x}, \, _{s_i}\boldsymbol{y}, \, _{s_i}\boldsymbol{z}]^{-1} \cdot \, _{w_i}\boldsymbol{R}_{s_i}^{-1} \end{aligned} \tag{19}$$

Equation 19 is then the solution for $_a\boldsymbol{R}_{o_i}$, where $_{w_i}\boldsymbol{R}_{s_i}$ is already known from the referencing step before.

3 Scalable, all-purpose reference specimen

The theoretical approach for the coordinate unification method has been explained in the section above. Thereby, some basic constraints on the structure and shape of an adequate reference specimen could already be derived:

– The same topography of the specimen has to be measurable by every sensor.
– At least one common marker point must be directly measurable or has to be derived from the overall shape.
– Every sensor has to be able to also measure the unique direction of any marker on the object.

Table 1: Optical measurement systems that are used for the presented referencing method.

System	NA	Field size (mm×mm)	Magnification	Lateral sampling (µm)	Surface suitability scattering (s), reflecting (r)
Fringe projection	0.125	9.7×6.7	1×	6.5	s ++, r −
Fringe projection	0.125	2.3×1.7	4×	1.6	s +, r −
Fringe projection	0.125	1.1×0.8	8×	0.8	s +, r −
White-light interferometer	0.55	0.1×0.1	50×	0.2	s +, r ++
Confocal	0.13	4.0×3.2	5×	3.3	s +, r +
Confocal	0.5	1.0×0.8	20×	1.6	s +, r +
Confocal	0.8	0.4×0.3	50×	0.3	s +, r +

The zoomable fringe projection microscope is a research device based on a *Leica MZ 12.5*, 1.0×*planapochromatic objective* [24], the white-light interferometer is a *Zygo, NewView 6300*, and the confocal measurement system is the device *Consigno* from *twip optical solutions*.

– The reference specimen must be highly scalable such that sensors with a wide spectrum of field sizes can achieve the given task.
– The surface of the specimen has to provide a certain roughness in order to also allow 3D shape measurements for structured light-based sensors.

The coordinate unification, presented in this paper, is applicable to microscopic sensors of different optical measurement principles. A list of exemplary sensors, the referencing has been tested with, is given in Table 1. Usually, a very popular and precise calibration target for referencing optical as well as tactile sensors within coordinate measurement machines (or similar) is a plate with at least three spherical reference gauges. In the literature, a very popular and precise calibration plate, which almost fulfills these requirements, is a sphere-plate artifact with at least three spheres, whose position is precisely known [20, 21]. However, it is very difficult to manufacture such a sphere plate that is still measurable with a white-light interferometer and fits into a field with a size lower than 200 µm. Especially, one will get into difficulties if it comes to the production of precise spheres with a diameter of a few tens of microns, as they must also have a matt surface for satisfying measurements with a fringe projection microscope.

Another possibility is the use of a pyramid as reference specimen [25], as its topography is highly scalable, such that sensors with a bigger field size and larger depth of focus can sample the entire pyramid, while precise sensors only register the top part of it. Nevertheless, the same problem holds for the pyramid artifact than for the sphere plate: It is almost impossible to produce a precise pyramid with a scattering surface whose topography has very low errors particularly in the top part, which is only visible to very precise sensors with a small field size and depth of focus.

The reference specimen, that is used for the presented unification approach, is depicted in Figure 4. It consists of a fused silica glass substrate (side length 45 mm) with a copper layer on top. The plate has a flatness below 1 µm, and the layer was originally totally reflecting. However, the roughness could be increased by means of a galvanic process with a subsequent oxidation. The measured roughness Sa of the surface is 18.1 nm (*Sensofar*, *S lynx*, *interferometric mode*, 50×, *NA* 0.55). This plate can be used as a planar calibration specimen for the zoomable fringe projection microscope. Additionally, its surface is also easily measurable by a white-light interferometer as well as a confocal microscope. Using this specimen, the plane of the copper layer is assumed to be the x-y-plane of the coordinate system {a}. The origin of this coordinate system including the x- and y-axes are given by a tiny cross structure. This cross, visible in Figure 5, has been cut into the surface by a focus ion beam milling (FIB, *FEI Helios NanoLab*) with an energy of 30 kV. Owing to the oxidation of the copper layer, no sufficient conductibility was available, such that a thin 10-nm gold layer has been sputtered before starting the focus ion beam process. This gold layer
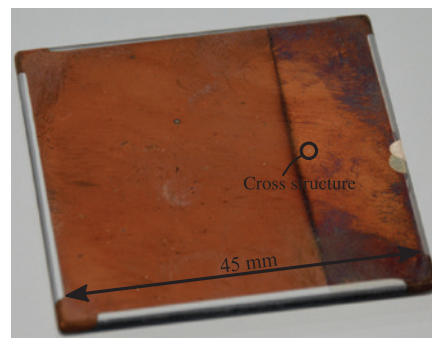

Figure 4: Image of the reference specimen for the coordinate unification of microscopic optical sensors. The specimen consists of a copper layer on top of a fused silica glass substrate (indicated flatness of below 1 µm, roughness Sa = 18.1 nm). A reflecting cross structure (see Figure 5) has been cut into the surface by focus ion beam milling.
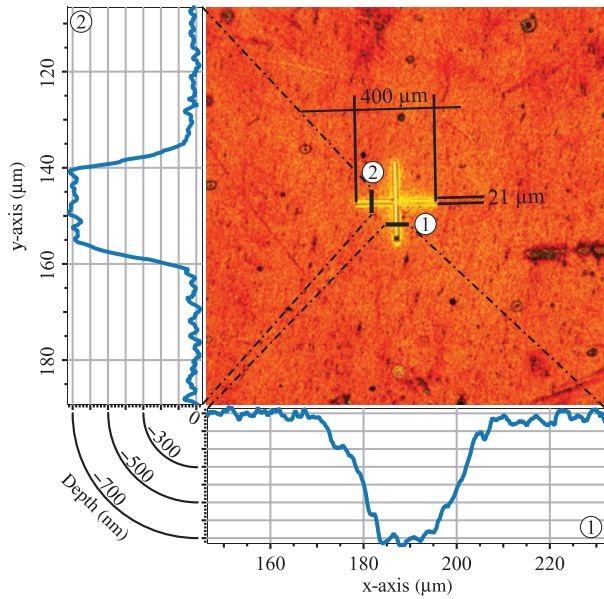
Figure 5: Microscopic image of the cross element in the reference specimen, used as marker for the coordinate system {*a*}. The line cut plots at the edges show two cross-sections over the marked arms of the milled cross.

is still visible in the right section of Figure 4; however, this thin layer does not badly influence the referencing process.

The length of the cross is 400 μm, which could also be extended but was mainly limited by the required manufacturing time of the FIB. The diameter of the arms is approximately 21 μm and the depth of the arms is around 700 nm.

The size of the cross has been chosen such that its topography can ideally be measured by microscopic sensors with higher numerical apertures. Nevertheless, sensors with lower NA or resolution (e.g. the fringe projection microscope or the 5× confocal sensor) can still obtain a high-contrast image of the reflecting cross if the intensity images of the acquired topography are considered. Figure 6 shows some exemplary measurements of the cross artifact using different optical sensors. Hereby, all available measurement principles as well as various field sizes were used for the demonstration. Especially in the case of the fringe projection, it is better to use the intensity image for detecting the center point of the cross than the topography image, as the highly reflecting cross structure leads to erroneous local height measurements of the fringe projection microscope, depending on the direction of the triangulation. The cross position is then fused with the topography image, which is used to obtain the *x-y* plane. While the white-light interferometer and the confocal microscope are commercial devices, the fringe projection microscope is a laboratory setup whose calibration is currently not traceable with respect to calibration standards.

4 Image and data processing

The main challenge of the presented referencing method is a robust and precise detection of the center and the
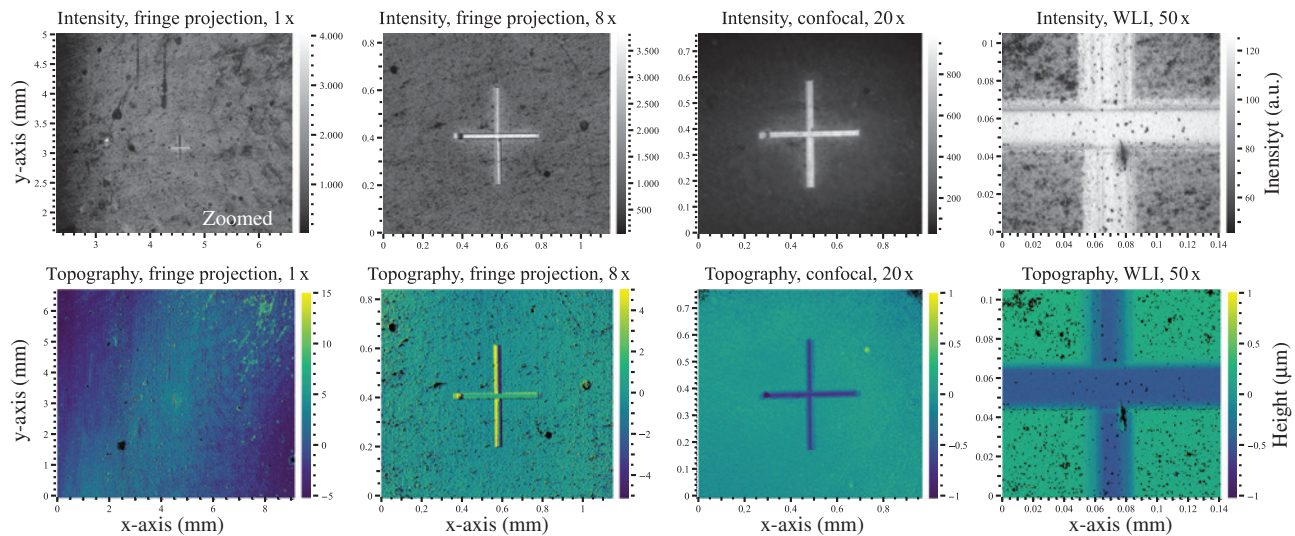

Figure 6: Sample measurements of the cross structure acquired with different optical measurement principles and scales. A systematic topography error is visible in the measurements of the 1× fringe projection measurements. The topography measurement of the 1× fringe projection shows some systematic errors due to a non-traceable calibration of this single sensor. Owing to the highly reflecting cross, the topography of the 8× fringe projection shows local errors. Therefore, the cross is only located in the intensity image for sensors based on structured-light projection.

orientation of the cross artifact as well as the fitted plane of the copper layer in order to safely determine the coordinate system $\{a\}$ in all acquisitions of the reference specimen. As can already be seen from the images in Figure 6, the quality and result of the acquisitions, given by multi-modal information channels like the topography, intensity, or contrast image, depend on the measurement principle as well as the resolution (or scale) of the applied sensor.

The presented image and data processing approach is able to handle these differences, although it is kept as general as possible. Besides the real measurement data, information about the coarse size and diameter of the cross as well as the sampling of the measurement device have to be given. The image processing then consists of the following steps:

- *A priori* information about the coarse pixel-based size and diameter of the cross is calculated. This is used by all the following steps.
- The given multi-modal measurement data are pre-selected and processed for the subsequent analysis.
- The coarse position and orientation of the cross is detected using a translation- and rotation-variant cross-correlation algorithm.
- A fine detection of all center points across the arms of the cross follows.
- A robust plane fit is applied to all topography values outside of the cross area.
- Two lines are fitted with respect to the sub-pixel point coordinates, indicating the *x*- and *y*-axes of the coordinate system $\{a\}$. The origin $_aQ$ of $\{a\}$ is given by the intersection of both lines. The normal vector of the fitted plane indicates the missing *z*-axis. The coordinate system is then fully determined with respect to the sensor frames $\{s_i\}$ or $\{c_i\}$.

Further details about the single steps are given in the following sections. The algorithm has been successfully tested with a 100% positive detection rate over more than 500 measurements acquired with all devices listed in Table 1.

4.1 Data pre-processing

This step is the only part of the entire data processing, which depends on the selected sensor and its resolution. Every optical sensor has to deliver at least one topography measurement of the reference specimen including the cross artifact. However, it is possible to use other data sources for the exact determination of the cross, its center point and orientation. These sources might be the topography, an optional contrast or intensity image. The selected source is pre-processed such that the center points of the arms of the cross artifacts have the highest values. In the case of the white-light interferometer, both the coarse and fine detection of the cross are executed on the basis of the topography image, which is inverted such that the trenches of the cross will be elevated. The fringe projection images are only analyzed using their intensity images. A special processing is further done for the measurement of the $1\times$ magnification level. The lateral resolution of this magnification is in the same range than the diameter of an arm of the cross. Owing to this undersampling, the arm, orientated along the triangulation plane, appears bright in the intensity image, whereas the perpendicular arm inversely dark (see Figure 7). For the confocal measurements, the contrast images are used for the selection of the coarse cross area, but the topography is analyzed within this coarse region for the sub-pixel precise fine search. If a topography image is used for the cross determination, a least-square plane is subtracted before starting the image processing, such that tilted acquisitions do not influence the analysis.
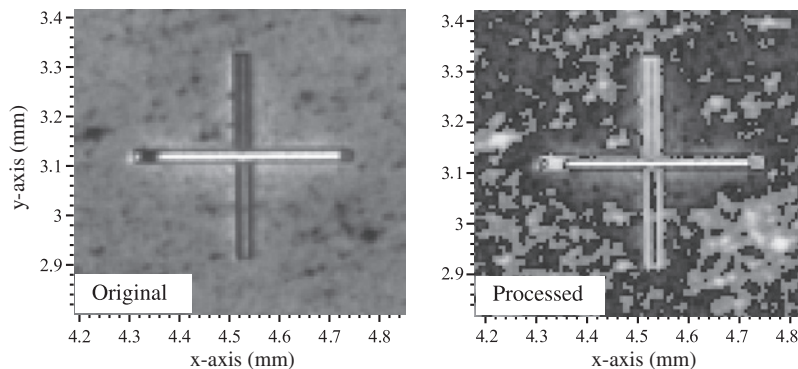

Figure 7: Image pre-processing of an under-resolved intensity image of the fringe projection microscope (magnification 1×).
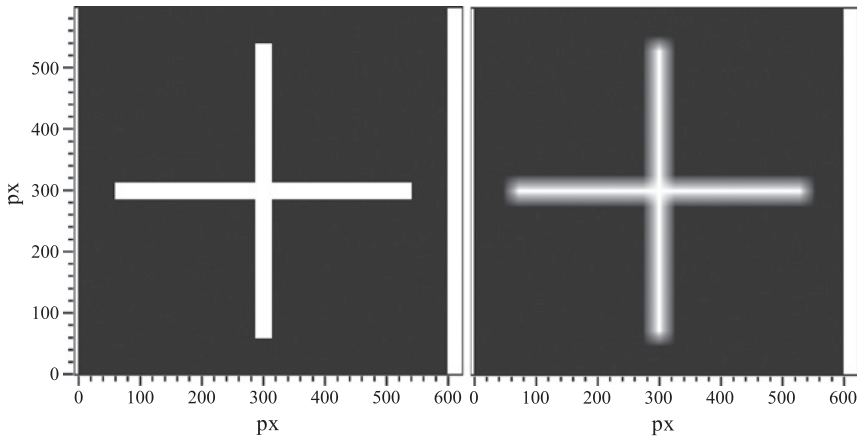
Figure 8: Template of the cross image auto-adapted for the 20× confocal sensor (left: original image, right: smoothed version for a more robust correlation).

4.2 Coarse cross detection

The coarse cross detection has the objective to roughly estimate the center position and orientation of the cross, which is especially necessary if the cross is smaller than the entire size of the sensor. At first, a coarse template image of the cross is created (see Figure 8). The size of the cross is given by *a priori* information, obtained in step 1. As image matching algorithms are badly influenced by high gradients in a template image, it is smoothed by a low-pass filter, whose kernel size linearly depends on the estimated diameter of an arm of the cross artifact.

The coarse template matching has to identify both the translation as well as rotation of the template with respect to the source image. Wilson and Theriot [26] presented a cross correlation method, which is both translation and rotation variant. In this method, the template and source images are at first Fourier transformed, as

that transformation is invariant to translated inputs but variant to rotations. Subsequently, the transformed images are converted to polar coordinates. Rotations lead to translations in polar coordinates along one axis, such that an ordinary cross correlation algorithm can be used to determine the rotation between template and source. In the next step, the template is rotated in image space by the given angle and another cross correlation between the original source image and the rotation template is executed in order to get the desired translation. Results of the entire processing are depicted in Figure 9.

4.3 Fine detection of the cross

Figure 10 shows a schematic for the sub-pixel fine detection of the cross artifact within the given input image. Owing to the coarse determination, four rectangular areas
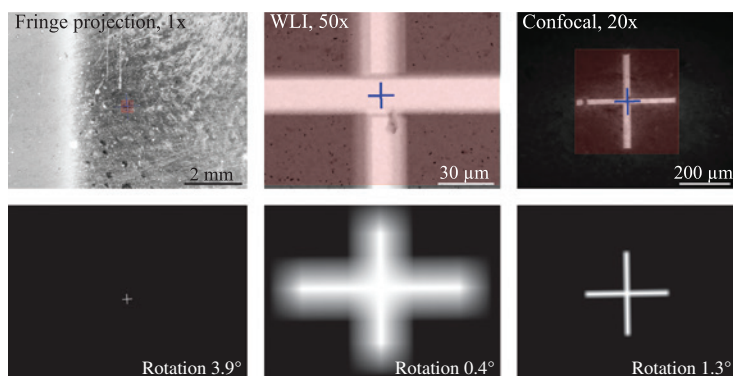

Figure 9: Results of the coarse cross registration using the two-step translation- and rotation-variant cross correlation. The red boxes in the real images above show the coarse position of the crosses. The template below is rotated by the determined rotation angle, which is a coarse, but sufficient, estimate of the real angle (especially for the fringe projection with low magnification).
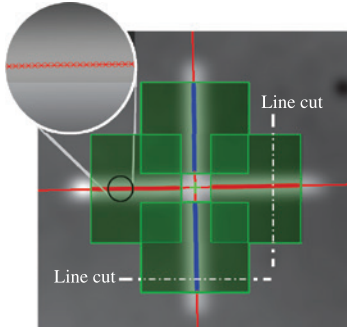
Figure 10: Fine detection of the cross structure with sub-pixel precision by evaluating line profiles (see Figure 11) within four rectangles. These are aligned over all four arms of the cross based on the information of the coarse detection. For a robust determination, the input source image is Gaussian smoothed before the detection. Finally, two perpendicular lines are fitted into all detected peak positions.

can be derived, which are centered over all four arms of the cross. Then, line profiles are extracted pixel-by-pixel within each rectangle. These profiles are oriented either in horizontal or vertical direction, such that they cross the underlying arm. In the next step, the sub-pixel precise peak position of every line segment is determined (see red or blue crosses in Figure 10). Finally, a Ransac-based line fit is applied to the set of blue and red crosses in order to get a robustly fitted line for the horizontal and vertical direction of the cross. The intersection point of both lines is the center point of the cross and, therefore, the origin of the desired coordinate system {a}.

The peak search in every line segment is depicted in Figure 11. The blue line indicates the original input profile (*here:* inverted topography, measured with the 20× confocal sensor). As this profile is noisy or a perpendicular profile cut across the arm of the cross might look like a rectangle (where it is difficult to find its center position), a Gaussian filter is applied to this profile, using the
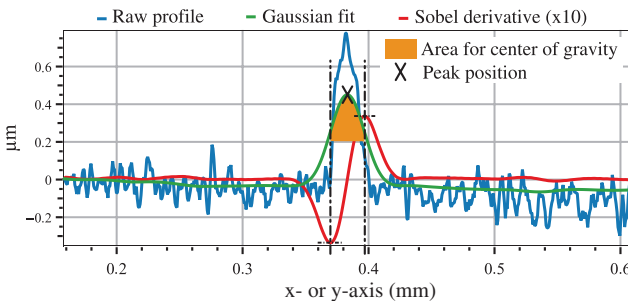
following filter kernel (shown in the y-direction only for the sake of convenience)

$$I(y) = \frac{1}{\sqrt{2\pi\sigma^2}} e^{-\left(\frac{y-y_0}{2\sigma}\right)^2}, \qquad (20)$$

where y is the pixel coordinate, y_0 is the current center pixel that should be replaced by its smoothed value, and σ^2 is the variance. σ is dependent on the lateral sampling rate of the sensor and is set to 1.1 times the coarse diameter of one arm of the cross (in pixels). In the next step, the derivative of the smoothed profile is calculated using the Scharr filter kernel, an optimized version of the Sobel operator [27]. The local peak positions of the derivative, that are close to the absolute maximum of the profile, determine the points of inflexion of the Gaussian smoothed profile. These points span the range, over which the center of gravity of the Gaussian profile is calculated in order to get the sub-pixel precise peak position. Its location corresponds to one blue or red cross in Figure 10.

4.4 Plane fit of topography

The last missing information to fully detect the coordinate system {a} within each sensor's coordinate system {s_i} is the plane of the copper layer. This is easily obtained by fitting a plane into all values of the topography, that do not belong to the cross area. In order to provide a robust plane fit, it is separated into two steps:

- A least-median fit is applied to all valid topography points outside of the cross. The least-median fit determines a plane where the median value of all distances between the fitted plane and the measured topography is minimized. This allows a robust and valid fit, even if up to 50% of all topography points are outliers and do not belong to the real plane [28].
- Based on the fitted plane, all values of the topography, whose distance to the plane is higher than a certain threshold value (e.g. 2 μm) are invalidated, and a final plane is fitted, using the method to minimize the sum of squared distances between all remaining points of the topography and the fitted plane.

Figure 11: Center-of-gravity-based peak determination along one horizontal or vertical line cut of the cross input image (see Figure 10).

5 Results

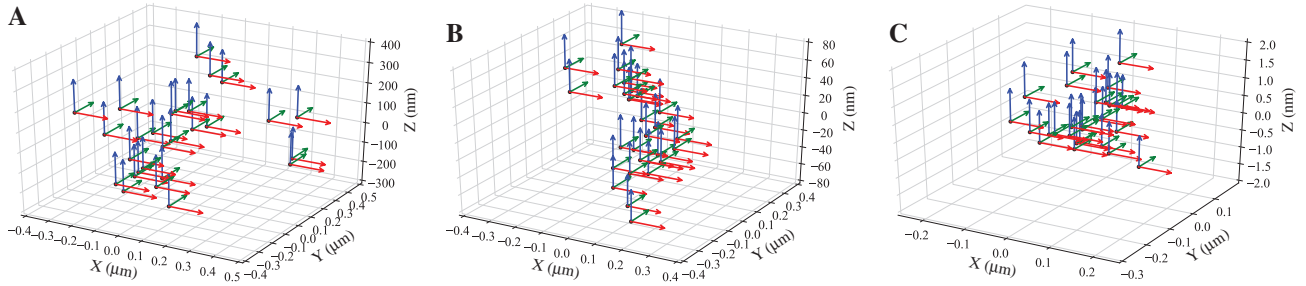After introducing the mathematical derivation as well as the necessary image- and data-processing steps for the

Figure 12: Detected center point and orientation of the cross artifact of 30 stationary measurements. (A) Fringe projection, 1×, (B) confocal microscope, 20×, (C) white-light interferometer, 50×.

multi-sensor coordinate referencing, some exemplary results are given in this section. For this, the data acquisition or data import, the image processing as well as the final analyses were done with the open-source software *itom* [29].

At first, 30 stationary measurements of the reference specimen have been conducted. The evaluated position and orientation of the cross artifact are depicted in Figure 12, represented by the origins of the displayed coordinate systems $\{a\}$. Table 2 contains the variance of both the position of the origin of $\{a\}$ (in the x, y, and z direction), as well as the azimuth and elevation angle of its orientation. The deviations of the center position are always below 10% of the lateral resolution of sensor (in the z direction yet smaller), such that a sufficient precision is reached.

The results in Figure 13 show the detected center points of the cross if the x-y stage of each sensor has been moved both in the x and y direction (in order to obtain the required rotation between the sensor's coordinate system and the perpendicular axes of the stage). In most cases, 15 positions have been set for each axis, besides the confocal measurements with the 5× and 20× objective, where 30 movements have been executed. The green and red lines are fitted into the single points using a Ransac-based line fit. The evaluated statistics are shown in Table 3. The normal vector has been determined by the cross product of the fitted x- and y-axes. Its tilt angle indicates the gradient of the stage with respect to the coordinate system $\{s_i\}$ of each sensor. The tilt between both axes indicates the reconstruction quality of the fitted lines based on detected center points in off-axis positions. The variance of the angle has been calculated in order to indicate the robustness of the line fit (*here:* in the y direction). For this determination, 750 random pairs of points of the 15 or 30 single measurements in the y direction have been selected, and a line was determined based on each pair. The variance value is the standard deviation over the angle difference between each line

and the overall best-fit line. It is clearly visible that this variance increases if the field size of the sensor decreases as the movement of the stage becomes very small, and imprecisions in these movements have a higher impact to the result. To improve this drawback, the method could be adapted such that the axis determination is also executable if only one arm of the cross is currently visible instead of its center point. Then, longer axis movements can be done to obtain more precise results.

In order to investigate the correctness and quality of the entire coordinate unification approach, a test object, depicted in Figure 14, has been measured by all exemplary measurement devices. The test object, itself, was fixed on a plate together with the reference specimen. This step is only necessary, as some of the involved sensors are desktop measurement systems and not integrated into the overall multi-axis inspection machine (see Figure 3). The test object itself is a laser-engraved aluminum plate, where the area within the red box has been acquired by means of a multi-scale measurement. If all sensors would be mounted in the same multi-axis machine, the referencing could be done in a pre-step, whereas the common acquisition of any object could be executed independently. Furthermore, the unknown rotation $_a\boldsymbol{R}_{o_i}$ between the cross

Table 2: Variance of the estimated position, elevation, and azimuth angles of the coordinate system $\{a\}$ of the reference specimen based on 30 static measurements for each sensor.

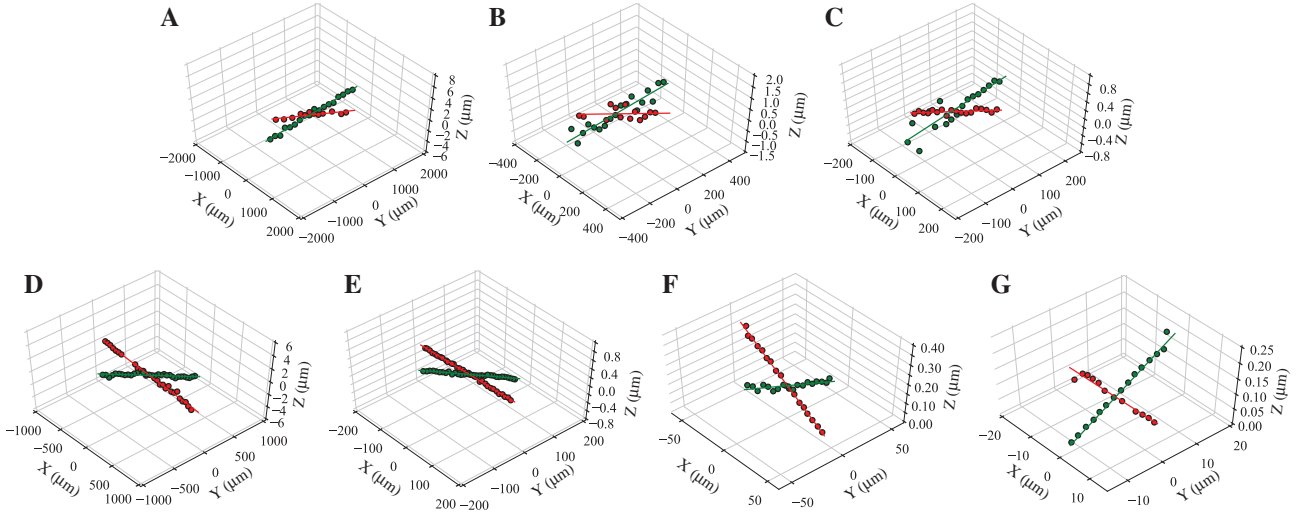| System	Variance (nm or ″)				
	X	**Y**	**Z**	**Elevation**	**Azimuth**
Fringe proj. 1×	158.7	199.2	142.5	13.3	189.9
Fringe proj. 4×	479.4	1203.4	321.8	17.0	32.9
Fringe proj. 8×	30.2	94.5	83.2	19.3	56.2
Confocal 5×	154.9	54.4	45.0	65.2	44.8
Confocal 20×	145.1	172.8	31.2	7.42	61.6
Confocal 50×	81.3	71.4	17.4	15.1	106.7
WLI 50×	52.2	99.2	0.8	3.9	65.7

Figure 13: Detected center points of the cross artifact upon a movement in the *x* and *y* directions of the stage of the device. The lines are fitted into these points using a Ransac-based line fit algorithm. (A, B, C) fringe projection microscope: 1×, 4×, 8× (D, E, F) confocal microscope: 5×, 20×, 50×, (F) white-light interferometer (WLI): 50×.

artifact and the coordinate system of the *x-y* stage has not to be determined, such that a more robust overall transformation is expected.

Figure 15 shows the reconstruction results of the measurements of the cross artifact during the referencing process. All single data sets are transformed to the common frame {*a*}. For a better representation, the topography values are separated by a 0.6-mm distance in the *z* direction. This also allows an overview about the scale range of the selected sensors. As expected, the depicted coordinate system {*a*} is located at the centers of the detected cross artifacts, and all topographies lie in its *x-y* plane. The color map represents the height values in the *z* direction. However, these values are separately adjusted for each data set in order to provide a clearer view.

The multi-scale measurement results of the exemplary object are depicted in Figures 16 and 17. While Figure 16 visualizes data sets in different colors according to the applied sensor and its configuration, the acquired topography in Figure 17 is encoded in a false color representation. Both images show the results of five different sensors. The overview image has been obtained by two single measurements of the 1× fringe projection microscope. More precise sensors up to the 50× confocal microscope and white-light interferometer were centered at two areas of the object. The zoomed images in the visualization show the fly through the scales located at the letter '*P*'. Owing to the lower numerical apertures, most sensors can only acquire surfaces with low gradients; however, the high-aperture measurements also allow acquisitions within very small fields of the side walls of the focused letter.

All in all, the results show good reconstruction results. Nevertheless, the overall transformation process is subject to a sensor-dependent uncertainty:

$$_a\boldsymbol{P} = (_a\boldsymbol{T}_{s_i} + \Delta_a\boldsymbol{T}_{s_i}) \cdot {}_{s_i}\boldsymbol{P}. \tag{21}$$

The translation part of the uncertainty matrix $\Delta_a\boldsymbol{T}_{s_i}$ is given by the *X*, *Y*, and *Z* variances of Table 2. If all sensors are mounted in the same multi-sensor setup, the uncertainty of the rotational components can be described by the angle variances of Table 3. The total uncertainty of the lateral position values, however, also depends on this rotational uncertainty multiplied by the distance between reference specimen and object (*here:* approximately 36 mm) due to the lever action. In case of the 8× fringe

Table 3: Results for the detected center positions of the reference specimen under distinct movements in the *x* and *y* direction of the stage.

System	Tilt of normal vector (°)	∠*x-y* axes (°)	Angle variance (°)
Fringe proj. 1×	0.21	89.99	0.01
Fringe proj. 4×	0.25	89.94	0.01
Fringe proj. 8×	0.23	89.96	0.01
Confocal 5×	0.31	89.99	0.01
Confocal 20×	0.25	89.97	0.02
Confocal 50×	0.25	89.94	0.07
WLI 50×	0.39	89.95	0.10

The angle variance is calculated over the directions of lines that are created by 750 randomly selected pairs of points out of all points along the *y*-axis.
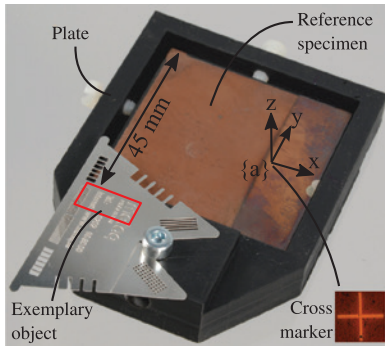
Figure 14: Image of the test plate that can be moved to different measurement systems and contains both an exemplary test object with some laser-engraved topographies as well as the reference specimen. If it is used in one single multi-sensor setup, the plate is not necessary, and the reference artifact as well as the object can be positioned independently on each other.
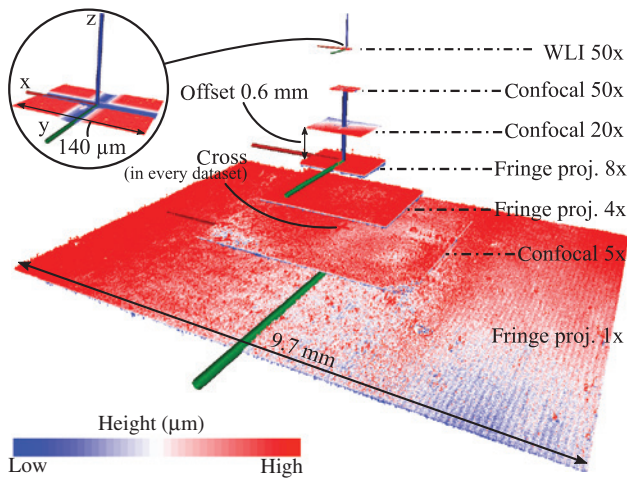

Figure 16: Measurement result of the test object (Figure 14). The measurements of each sensor and scale are visualized by different colors.

Figure 15: View to measurements of the reference specimen, transformed to the destination coordinate system {a}. For a better representation, all measurements have been moved by 0.6 mm in the z direction each. The color map encodes the z-values; however, its range is separately adjusted for each data set.
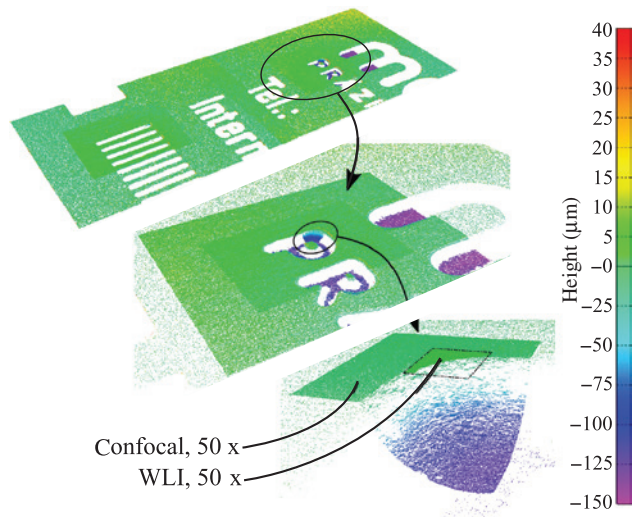
Figure 17: Measurement result of the test object (Figure 14). The topography is encoded in the color information with respect to the base plane of the exemplary object.

projection microscope, the total position uncertainty U after the transformation is

$$U = 94.5\,\text{nm} + \tan(0.01°) \cdot 36\,\text{mm} = 6.4\,\mu\text{m}.$$

For finer reconstruction results, it is afterward possible to apply a fine adjustment based on stitching or feature-based matching algorithm [6].

6 Conclusion

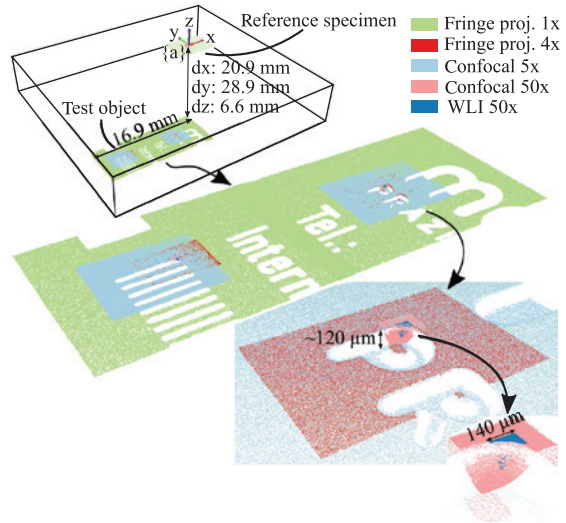In this paper, we presented a coordinate unification approach for multi-scale optical sensor systems. The addressed sensors have resolutions in the nanometer to millimeter range and can sample arbitrary surfaces by various optical measurement principles. An adapted reference specimen has been designed, which is used for the referencing of these sensors. For the evaluation of this object, a dedicated image processing routine has been developed that mainly depends on the sampling distance or the scale value of each sensor. The overall sensor referencing has been implemented and tested using a zoomable fringe-projection microscope, a confocal microscope, as well as a white-light interferometer.

The presented reference specimen is mainly usable for various optical profilometers that are able to measure the topography of a scattering plane object as well as identify the position and orientation of the cross within the plane. A coordinate unification of other optical sensors, like for instance OCT or strain measurement systems, is only possible if they allow resolving the topography of this reference specimen by a secondary measurement mode. In general, the approach is not only limited to one single reference specimen. It is feasible to use several specimens, adapted to further types of sensors, under the prerequisite that all specimens are precisely calibrated to each other with respect to the position and orientation of their specific feature points.

In the current approach, any imperfections of the positioning of the motor stages or axes have been neglected such that high-precision axes with internal control feedback systems are required. In order to improve the unification quality and give more details about the overall uncertainty, further investigations concerning the influence of the mechanical properties of the setup have to be done.

References

[1] W. Osten, Proc. SPIE 9960, 99600P (2016).

[2] W. Osten, in 'Optical Imaging and Metrology', Ed. By W. Osten and N. Reingand (Wiley-WCH, Berlin, 2012).

[3] J. Siepmann, M. Heinze, P. Kühmstedt and G. Notni, Proc. SPIE 7432, 74320Y (2009).

[4] R. Schmitt, M. Uekita and K. Vielhaber, Meas. Sci. Technol. 20, 117003 (2009).

[5] W. Osten, P. Andrä and D. Kayser, Technisches Messen 66, 413–428 (1999).

[6] A. Weckenmann, X. Jiang, K.-D. Sommer, U. Neuschaefer-Rube, J. Seewig, et al., CIRP Ann. – Manuf. Technol. 58, 701–721 (2009).

[7] H. F. Durrant-Whyte, Int. J. Rob. Res. 7, 97–113 (1988).

[8] H. Ruser and F. Puente León, tm – Technisches Messen 74, 93–102 (2007).

[9] W. Osten and N. Reingand, editors. in 'Optical Imaging and Metrology', (Wiley-WCH, Berlin, 2012).

[10] K. Gastinger and W. Osten, in 'Imaging and Applied Optics', (Optical Society of America, Arlington, 2013) pp. ATu2B.1.

[11] K. Gastinger, L. Johnsen, M. Kujawinska, M. Jozwik, U. Zeitner, et al., Proc. SPIE 7718, 77180F (2010).

[12] D. Kayser, T. Bothe and W. Osten, Opt. Eng. 43, 2469–2477 (2004).

[13] W. Lyda, A. Burla, T. Haist, J. Zimmermann, W. Osten, et al. Proc. SPIE 7718, 77180G (2010).

[14] W. Lyda, A. Burla, T. Haist, M. Gronle and W. Osten, Int. J. Precis. Eng. Man. 13, 483–489 (2012).

[15] F. Franceschini, M. Galetto, D. Maisano and L. Mastrogiacomo, Int. J. Precis. Eng. Manuf. 15, 1739–1758 (2014).

[16] J. Böhm, J. Gühring and C. Brenner, Proc. SPIE 4309, 154–161 (2001).

[17] A. Loderer and T. Hausotte, J. Sens. Sens. Syst. 5, 1–8 (2016).

[18] S. Rusinkiewicz and M. Levoy, in 'Proc. 3rd Int. Conf. on 3-D Digital Imaging and Modeling', 3, 145–152 (2001).

[19] Y. Huang, X. Qian and S. Chen, Comput. Aided Des. 41, 240–255 (2009).

[20] F. Li, A. P. Longstaff, S. Fletcher and A. Myers, Opt. Laser Eng. 55, 189–196 (2014).

[21] D. Wang, W. Tang, X. Zhang, Q. Ma, J. Wang, et al. Proc. ICMA, 1761–1766 (2015).

[22] A. Keck, M. Böhm, K. L. Knierim, O. Sawodny, M. Gronle, et al., Technisches Messen 81, 280–288 (2014).

[23] W. Kabsch, Acta Crystallogr. 32, 922–923 (1976).

[24] X. Schwab, C. Kohler, K. Körner, N. Eichhorn and W. Osten. Proc. SPIE 6995, 69950Q (2008).

[25] M. Gronle, W. Lyda, A. Burla and W. Osten, Proc. SPIE 8430, 84300J (2012).

[26] C. A. Wilson and J. A. Theriot, IEEE Trans. Image Process. 15, 1939–1951 (2006).

[27] B. Jähne, H. Scharr and S. Körkel, in 'Handbook of Computer Vision and Applications', Ed. By B. Jähne, H. Haußecker and P. Geißler, volume 2 (Academic Press, San Diego and London, 1999) pp. 125–151.

[28] P. J. Rousseeuw, J. Am. Stat. Assoc. 79, 871–880 (1984).

[29] M. Gronle, W. Lyda, M. Wilke, C. Kohler and W. Osten, Appl. Opt. 53, 2974 (2014).

Marc Gronle
Institut für Technische Optik, Universität Stuttgart, Pfaffenwaldring 9, 70569 Stuttgart, Germany
gronle@ito.uni-stuttgart.de

Marc Gronle received his Diploma in Mechatronics from the University of Stuttgart in 2011. Since Mai 2011 he is employed at the Institute of Applied Optics (ITO) at University of Stuttgart as research assistant. From October 2014 on, he is heading the group of 3D metrology. His research work is focused on multi-sensor optical systems, 3D view and automatic measurement planning as well as sensor technologies and image processing for 3D metrology. Furthermore, he is leading the development team for the open source lab automation and measurement software *itom*.

Wolfgang Osten
Institut für Technische Optik, Universität
Stuttgart, Pfaffenwaldring 9, 70569
Stuttgart, Germany

Wolfgang Osten received the Diploma in Physics from the Friedrich-Schiller-University Jena in 1979 and in 1983 the PhD degree from the Martin-Luther-University Halle-Wittenberg for his thesis in the field of holographic interferometry. From 1984 to 1991 he was employed at the Central Institute of Cybernetics and Information Processes in Berlin making investigations in digital image processing and computer vision. In 1991 he joined the Bremen Institute of Applied Beam Technology (BIAS) to establish the Department Optical 3D-Metrology. Since September 2002 he has been a full professor at the University of Stuttgart and director of the Institute for Applied Optics. His research work is focused on new concepts for industrial inspection and metrology by combining modern principles of optical metrology, sensor technology and image processing. Special attention is directed to the development of resolution enhanced technologies for the investigation of micro and nano structures.